Rational Design of Hierarchical, Porous, Co-Supported, N-Doped Carbon Architectures as Electrocatalyst for Oxygen Reduction

Mengfei Qiao, Ying Wang, Xamxikamar Mamat, Anran Chen, Guoan Zou, Lei Li, Guangzhi Hu, Shusheng Zhang, Xun Hu, Damien Voiry

CHEMISTRY & SUSTAINABILITY

CHEMSUSCHEM

ENERGY & MATERIALS

Accepted Article

Title: Rational Design of Hierarchical Porous Cobalt, Nitrogen-doped Carbon Architectures as Efficient Oxygen Reduction Reaction Electrocatalysts

Authors: Damien Voiry, Mengfei Qiao, Ying Wang, Xamxikamar Mamat, Anran Chen, Guoan Zou, Lei Li, Guangzhi Hu, Shusheng Zhang, and Xun Hu

To be cited as: *ChemSusChem* 10.1002/cssc.201903053

Link to VoR: http://dx.doi.org/10.1002/cssc.201903053

A Journal of

ChemPubSoc Europe

WILEY-VCH

www.chemsuschem.org

Rational Design of Hierarchical Porous Cobalt, Nitrogen-doped Carbon Architectures as Efficient Oxygen Reduction Reaction Electrocatalysts

Mengfei Qiao,‡[a,g] Ying Wang,‡[a] Xamxikamar Mamat,‡[a] Anran Chen,[b] Guoan Zou,[a] Lei Li,*[c] Guangzhi Hu,*[a,b,c] Shusheng Zhang,[d] Xun Hu,[e] and Damien Voiry,*[f]

Abstract: Developing highly active non-precious metal catalysts for the oxygen reduction reaction (ORR) is of great significance to reduce the cost of fuel cells. Three-dimensional ordered porous structures could substantially improve the performance of the catalysts because of its excellent mass diffusion properties and high specific surface area. Herein, we prepared ordered porous ZIF-67 by forced molding of a polystyrene template and obtained cobalt-supported, nitrogen-doped three-dimensional ordered porous carbon (Co-NOPC) after further carbonation. The resultant Co-NOPC exhibits excellent performance for the ORR in an alkaline medium with a half-wave potential ($E_{1/2}$) of 0.86 V vs. RHE, which is greater than that of the state-of-the-art Pt/C (0.85V vs. RHE). Moreover, the substantially improved catalytic performance of Co-NOPC compared to cobalt-supported, nitrogen-doped carbon (Co-NC) reveals the key role of its hierarchical porosity for boosting ORR. Co-NOPC also performs a close-to-ideal four-electron transfer path, long-term durability, and methanol penetration resistance, making it promising for large-scale application.

Introduction

In recent decades, issues such as energy shortage and environmental pollution due to the extensive exploitation and utilization of fossil fuels have stimulated the development of new energy materials and energy conversion technologies.[1] With the advantages of high energy density, environmental friendliness, easy implementation, and unlimited sources of reactants, proton exchange membrane fuel cells (PEMFCs) are expected to play an important role in next-generation energy technologies.[2] One major bottleneck to the commercial application of PEMFCs lies in the insufficient activity and durability of the electrocatalysts to accelerate the sluggish kinetics of the oxygen reduction reaction (ORR) at the cathode.[3] For high-performance catalysts, most theoretical and experimental studies believe that the active sites should have an intermediate adsorption strength for the reactant and its intermediates to reduce reaction barrier, and the substrate should have a high specific surface area and rich pore structure, thus achieving rapid mass transfer on electrode surface.[4] Meeting all these conditions is a major bottleneck in the search for ideal ORR catalysts. Notably, the control of the porosity in order to optimize both the surface area and the efficient diffusion of the O_2 to the active sites request the preparation of catalytic materials with hierarchical porosity.[5] State-of-the-art catalysts Pt/C, wherein Pt nanoparticles are supported on high-surface-area carbon, exhibit a relatively low overpotential and ideal four-electron transmission path for the ORR.[6] However, the high cost, resource constraints, poor stability and nonresistance to methanol penetration, hinder its large-scale application, necessitating the search for a better alternative.[7] Based on current research, metal–nitrogen–carbon (M–N–C) catalysts, where M denotes a transition metal (typically with M = Fe or Co), are the most promising low-cost substitutes for Pt-based catalysts.[8] Fe-N-C catalysts show the highest

[a] M.F.Qiao, Y.Wang, X. Mamat, Prof. G.A.Zou, Prof. G.Z.hu
Key Laboratory of Chemistry of Plant Resources in Arid Regions State Key Laboratory Basis of Xinjiang Indigenous Medicinal Plants Resource Utilization, Xinjiang Technical,Institute of Physics and Chemistry,Chinese Academy of Science
Urumqi 830011, China.
Emali : guangzhihu@ynu.edu.cn

[b] Dr. A.R.Chen, Prof. G.Z.hu
School of Chemical Science and Technology, School of Energy, Yunnan University,Kunming 650091, China

[c] Prof. L.li, Prof. G.Z.hu
College of Biological, Chemical Sciences and Engineering, Jiaxing University
Emali : leili@mail.zjxu.edu.cn

[d] Prof. S.S.Zhang
College of Chemistry and Molecular Engineering, Zhengzhou University Zhengzhou, 450000, China.

[e] Prof. X.Hu
School of Material Science and Engineering,University of Jinan, Jinan 250022, China.

[f] Prof. D. Voiry
Institut Européen des Membranes, IEM, UMR 5635, Université Montpellier, ENSCM, CNRS, 34095 Montpellier Cedex5, France
Emali: damien.voiry@umontpellier.fr

[g] M.F.Qiao
University of Chinese Academy of Sciences, Beijing 100049, China.

‡ Those authors contributed equally to the work.

activity among all M–N–C materials, but the Fenton reactions (Fe^{2+} + H_2O_2), where dissolved Fe ions combine with H_2O_2, will generate significant amounts of active oxygen-containing hydroxyl and hydroperoxyl radicals, thereby leading to the irreversible erosion and degradation of the electrodes and diaphragm.[9] Therefore, Co-N-C based catalysts may be a promising substitute for Pt/C when considering both, a high catalytic activity and operational stability over reasonable service life.[10]

In order to achieve a breakthrough in performance, many inspiring works have focused on obtaining a perfect combination of Co-N-C structure and excellent substrate materials.[11] Recently, metal–organic frameworks (MOFs), which possess structural diversity, easy functionalization and high specific surface area, have been selected as a self-sacrificing precursor/template for preparing nanoporous carbons.[12] Among the MOFs, ZIF-67, which consists of Co^{2+} and 2-medetomidine, has received wide attention owing to easy synthesis, high porosity of the zeolite-like topology, and particularly it could be an ideal source of carbon and nitrogen. The coordination structure of Co^{2+} and 2-methylimidazole can be in situ-transformed into a Co-N_x structure, and the pore structure can be well inherited during the pyrolysis of ZIF-67, which endows it with high intrinsic activity and active site stability.[13] However, their catalytic activity is limited because of deep burial of the active sites and low mass transfer of inherit microporous structure of ZIF-67, which stimulates the researcher to resolve this problem by combining with excellent conductive and high surface area carbon materials such as graphene, carbon nanofibers etc..[14] Shen et al. reported a kind of ZIF-67 and reduced graphene oxide derived carbon composite named ZIF-C/rGO, where the rGO integration led to better charge transfer channels and more micropores to load active sites.[15] Yin et al. synthesized ZIF-67/PAN by the in-situ growth of ZIF-67 nanocrystals on PAN fibers, and further carbonized it at 800 °C to obtain ZIF-67/PAN-800, which also showed significantly improved performance.[16] Although these attempts have improved the catalytic performance of oxygen reduction to a certain extent, they have failed to achieved benchmarks from practical applications. Introducing macropores into ZIF-67 should be a good idea to achieve efficient utilization of active sites by exposing more surfaces, meanwhile, macro/mesopores will also improve the mass transfer of macromolecules near the double layer.[17]

Herein, we demonstrate the successful synthesis of porous ZIF-67 (OP-ZIF-67) with the accurate control of the macro and microporosity by developing an original approach that combines hard template method and ultrasonic nucleation.[18] The ordered MOF superstructure translates, after carbonization, into optimized hierarchical order macro-microporous carbon skeleton for electrocatalytic materials, enabling efficient diffusion of the reactant to the actives while maximizing the density of active sites. The resultant carbonized product, cobalt-supported, nitrogen-doped three-dimensional ordered porous carbon (Co-NOPC), exhibits enhanced catalytic activity and long-term stability towards ORR under both acidic and alkaline conditions. The half-wave potential of the obtained Co-NOPC was 0.86 V vs. RHE in 0.1M KOH electrolyte, which is substantially greater than the 0.80 V vs. RHE of the cobalt-supported, nitrogen-doped carbon catalysts (Co-NC) obtained by carbonizing well-defined ZIF-67. The enhanced ORR activity of Co-NOPC is attributed to the high intrinsic activity of the Co-N_x structure, adequate active sites exposed by the higher specific surface area, and a higher diffusion speed imparted by the orderly three-dimensional porous structure. Significantly, our study shed light on an innovative approach for enhancing the performance towards ORR or other electrocatalytic reaction based on MOF-derived materials.

Results and Discussion

The method for the synthesis of Co-NOPC is illustrated in Figure 1a. First, polystyrene spheres (PS) templates were fully immersed in a methanol solution of cobalt nitrate hexahydrate and 2-methylimidazole. After ultrasonic nucleation and static growth at room temperature, PS@ZIF-67, which is a mixture of PS and ZIF-67, was prepared. Then, the precursor OP-ZIF-67 was then obtained by repeatedly washing with tetrahydrofuran (THF) to remove the PS template. The OP-ZIF-67 engraved reversely by the PS template has a three-dimensional ordered porous structure. After further carbonation at 500 °C, the cobalt, nitrogen-doped ordered porous carbon catalysts (Co-NOPC) was finally obtained with well-preserved porous structure of the precursor. The ordered porous structure of Co-NOPC with the combination of macro/meso/micropores is expected to not only provide a high specific surface area to load enough active sites, but also facilitates the mass transfer process. On the other hand,

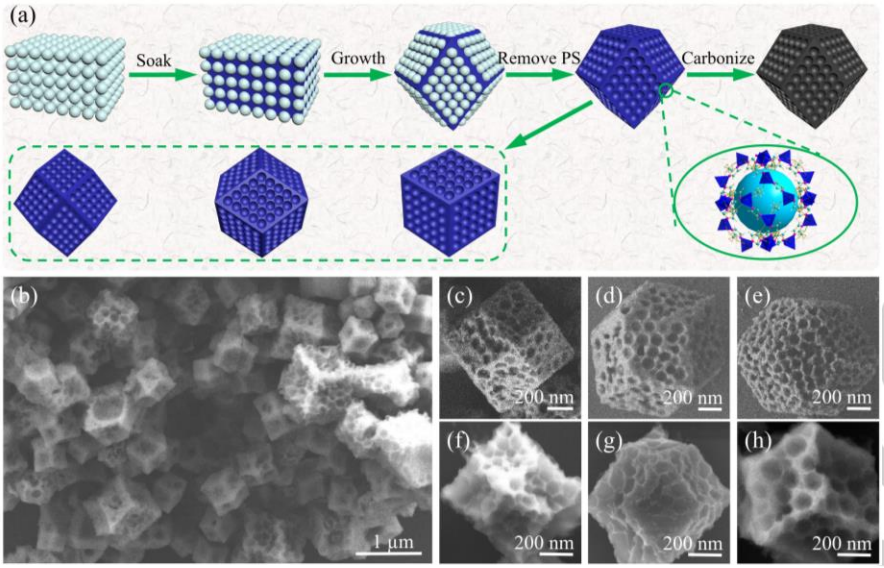

Figure 1. (a) Schematic of the Co-NOPC synthesis. (b) SEM images of the Co-NOPC. (c-e) SEM images of OP-ZIF-67. (f-h) SEM images of Co-NOPC.

the Co-N_x active sites obtained by the in-situ conversion of Co^{2+} and 2-methylimidazole complexes confer to the catalyst high intrinsic activity and long-term stability.

To get information on the morphology and structure, the pristine OP-ZIF-67 and the carbonized Co-NOPC were investigated by field-emission scanning electron microscopy (FESEM) and high-resolution transmission electron microscopy (HRTEM). Figure 1c-e shows the typical SEM images of OP-ZIF-67 at various magnifications. OP-ZIF-67 is found to adopt a well-defined rhombic dodecahedron morphology with a particle size of 1 μm, where macropores of approximately 110 nm are regularly distributed throughout the single-crystal particles. Additionally, the Co-NOPC, obtained by the further carbonation of OP-ZIF-67 at 500 °C, was characterized by SEM (Figure 1b, f-h). Although there is a certain degree of collapses, the pore structure and morphology are vastly consistent with those of the precursor. The internal structure of OP-ZIF-67 characterized by HRTEM (Figure 2a-c) further revealed that the macropores are regularly distributed throughout the single-crystal particles, which were engraved reversely by the PS template (Figure S2). After thermal treatment at 500 °C, the crystal surface (Figure 2d-f) becomes no longer smooth as before, and the hierarchical ordered macro-micropore transform into inter-connected carbon skeleton. The relatively disordered carbon phase (Figure 2f) implies that abundant defects, such as vacancies, dislocations and shear defects in favor of ORR catalysis exist in the carbon structure.[19] The EDS mapping in Figure 2g demonstrate that no dramatic migration and aggregation of metallic Co occurs after pyrolysis, which is attributed to the in-situ conversion of coordination of Co and N under mild conditions.[20] For comparison, the morphology of conventional ZIF-67 and carbonation derivative (Co-NC) were also investigated in Figure S3.

Figure 3a shows the X-ray diffraction (XRD) patterns of ZIF-67, OP-ZIF-67 and simulated ZIF-67. The consistency of peak types among the three samples confirms that ZIF-67 and OP-ZIF-67 both formed a complete crystal structure with no impurity phase in the materials.[21] The XRD patterns of the final samples of Co-NOPC and Co-NC are shown in Figure 3b. The diffraction peaks appearing at approximately 23.3° and 43.5° can be assigned to the (002) and (100) planes of the graphite structure.[22] Moreover, there are no significant metal peaks in XRD, which indicates that no obvious metal nanoparticles were formed after annealing at 500 °C. Furthermore, the XRD patterns of the catalysts synthesized at different temperatures are compared in Figure S4. The Co-

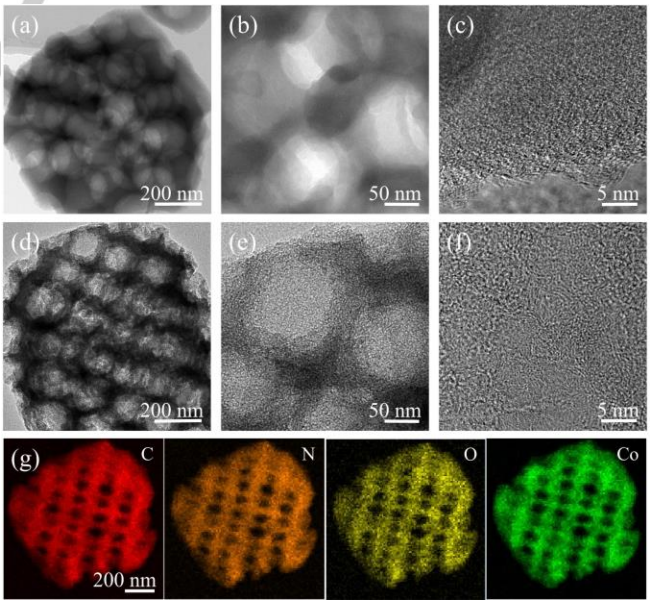

Figure 2. (a-c) HRTEM images of OP-ZIF-67. (d-f) HRTEM images of Co-NOPC. (g) EDS mapping of Co-NOPC.

NOPC-500, Co-NOPC-600, and Co-NOPC-700 were derived

from the same precursor OP-ZIF-67-3:4, where 3:4 represents the mass ratio of $Co(NO_3)_2 \cdot 6H_2O$ and 2-methylimidazole, but annealed at different temperatures of 500 °C, 600 °C, and 700 °C, respectively. The apparent metal peaks of Co for Co-NOPC-600 and Co-NOPC-700 suggest an intensity reduction from Co^{2+} to Co^0 and inevitable aggregation of the metal atoms when the carbonation temperature exceeds 600 °C, which will result in a decrease of the active sites.[23]

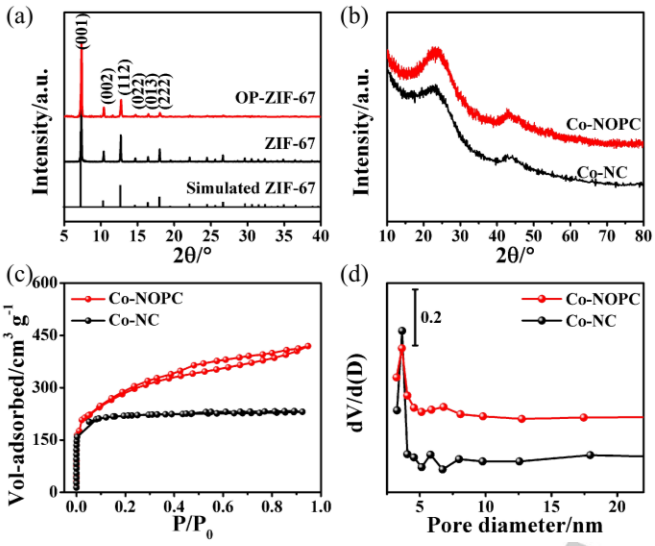

Figure 3. (a) XRD patterns of the precursors ZIF-67 and OP-ZIF-67. (b) XRD patterns of the catalysts Co-NC and Co-NOPC. (c) Nitrogen adsorption-desorption isotherms and (d) corresponding pore size distributions of Co-NOPC and Co-NC.

To further investigate the influence of the pyrolysis temperature on the structure of the catalyst, nitrogen adsorption experiments were performed for comparing the specific surface area and pore size distribution of the samples synthesized at different temperatures. Co-NOPC-500, which was annealed at 500 °C, had a better nitrogen physical adsorption capacity compared with the samples synthesized at 600 °C or 700 °C (Figure S5). The BET surface areas of Co-NOPC-500, Co-NOPC-600, and Co-NOPC-700 are 418 $m^2 g^{-1}$, 362 $m^2 g^{-1}$, and 314 $m^2 g^{-1}$, respectively. The similar isotherms for Co-NOPC and Co-NC at low pressure indicate a similar microporous structure (Figure 3c), whereas the pore size distribution curves (Figure 3d) illustrate that both Co-NOPC and Co-NC have abundant mesopores with a pore size of ~3.6 nm, which are formed during pyrolysis. These results show that the introduction of macropores has no significant effect on the formation of micropores and mesopores. We believe that the mesoporosity originates from the structure of the ZIF-67 and forms during the graphitization process. However, a higher specific surface area of Co-NOPC (418 $m^2 g^{-1}$) compared with that of Co-NC (214 $m^2 g^{-1}$) confirms that ordered macropores are responsible for the increased specific surface area. Raman spectra were analyzed to characterize the change in the carbon phase with the synthesis temperature (Figure S6). The higher I_D/I_G ratio of Co-NOPC-500 reveals that an over-high temperature will reduce the defect positions which are typically active site centers.[25] This result agrees well with that of XRD, in that Co^{2+} will be quickly reduced to Co^0 with increasing temperature, and that the recombination of chemical bonds will also reduce the number of active sites.[26]

The catalysts obtained at different temperature were characterized and compared by X-ray photoelectron spectroscopy (XPS).[27] The survey of Co-NOPC (Figure S7, Table S1 and Table S2) reveals the presence of C 1s, N 1s, O 1s, and Co 2p elements, without any impurities. The content of N 1s, O 1s, and Co 2p decrease while the content of C 1s increases with the increasing pyrolysis temperature. The high-resolution XPS spectrum of Co $2p^{3/2}$ (Figure 4a) can be fitted into two components, corresponding to Co^0 (776.9 eV) and Co^{2+} (779.1 eV).[28] Co^{2+} is known to be more beneficial to the catalytic activity when in the form of coordinated Co-N_x obtained through the in-situ transformation of the coordination structure of Co^{2+} and 2-methylimidazole. On the other hand, Co^0, obtained through the reduction product of Co^{2+}, tends to agglomeration and lose its ORR activity.[29] The relative proportion of Co^{2+} over Co(0) reduces from 91.5% to 68.6% when the annealing temperature increases from 500 °C to 700 °C, verifying the advantage of mild-temperature graphitization (Figure 4c). To precisely determine the close relationship between active site centers and chemical environment of the doped nitrogen, the N 1s spectra of all the samples with different pyrolysis temperatures were analyzed. Figure 4b shows that the high-resolution N 1s spectrum split into four subpeaks at 397.3 eV, 398.1 eV, 399.2 eV and 401.6 eV, corresponding to pyridinic (Py-N), pyrrolic (Pyr-N), graphitic like (Gra-N), and oxidized type (Oxi-N) nitrogen, respectively. According to the literature, Py-N and Gra-N can effectively boost oxygen adsorption to reduce the ORR overpotential because of their excellent electron-accepting abilities.[30] According to the literature, Py-N and Gra-N can effectively boost oxygen adsorption to reduce the ORR overpotential because of their excellent electron-accepting

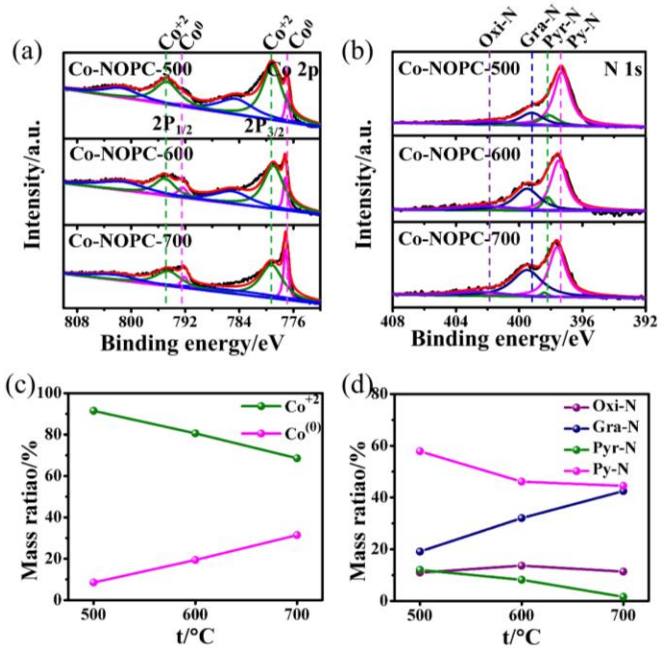

Figure 4. The fine spectra of (a) Co 2p and (b) N 1s of Co-NOPC synthesized at different temperatures. (c) Corresponding fitting mass ratio of Co^{2+} and Co^{0}. (d) Corresponding fitting mass ratio of N with different chemical structures.

abilities. [31] In addition, part of pyridinic N and pyrrolic N atoms can serve as coordination sites for Co in the form of N-coordinated Co structures: Co-N_x (x = 2 and 4) as previously identified using X-ray absorption spectroscopy (XAS) and Mössbauer spectroscopy[.[19,32] Density functional theory (DFT) in agreement with experimental studies has suggested that Co-Nx has a lower energy barrier for oxygen dissociation and thus acts as active site in the catalytic ORR process from Co-N-C based catalysts [10b, 11, 29] As shown in the Figure 4d, the ratios of Py-N and Pyr-N in Co-NOPC rapidly decrease with the increase of annealing temperature. On the other hand, the rapid growth of Gra-N signals at increasing annealing temperature verifies the results of Raman spectra. In order to optimize catalytic performance, we adjusted the ratio of precursors for the synthesis of Co-NOPC. A series of OP-ZIF-67 typed materials was synthesized with different ratios of Co^{2+} and 2-methylimidazole precursor and named as OP-ZIF-67-n:m, where n:m represents the feeding mass ratios of $Co(NO_3)_2{\cdot}6H_2O$:2-methylimidazole. We found that the regular single crystal structure of ZIF-67 with ordered porosity was only formed at the mass ratios of 3:4 of $Co(NO_3)_2{\cdot}6H_2O$:2-methylimidazole. Our analyses also reveal that a low cobalt mass ratio does not lead to the growth of single crystal MOF particles while a high cobalt mass ratio may lead to the uncontrolled shapes of crystal particles (Figure S8). Furthermore, we evaluated the effect of feed amount of $Co(NO_3)_2{\cdot}6H_2O$ to active sites using XPS (Figure S9). The proportion of Co-N_x also tends to increase with increasing Co content, and reaches the maximum when the ratio of $Co(NO_3)_2{\cdot}6H_2O$ and 2-methylimidazole is 3:4. In addition, compared to controlled sample Co-NC, Co-NOPC-3:4 had a higher fitting Co^{2+}/Co^{0} ratio, which might be related to a better coordination structures. All these evidences suggest that Co-NOPC-3:4 is the most suitable candidate for the oxygen evolution reaction.

The catalytic performance of Co-NOPC and Co-NC samples for ORR were firstly evaluated in O_2-saturated 0.1 M KOH on a rotating disk electrode (RDE) at a sweep rate of 10 mV s^{-1} and a rotation rate of 1600 rpm. The cyclic voltammetry (CV) measurements were employed to evaluate the ORR catalytic activity of the as-prepared catalysts and the benchmark Pt/C (20 wt.%) catalyst (Figure S10). The CV curves of all the tested catalysts showed obvious oxygen reduction peaks in O_2-saturated electrolytes, whereas featureless CV curves were obtained in N_2-saturated electrolytes. Notably, the more positive reduction peak potential of Co-NOPC (0.83 V), compared to 0.80 V and 0.83 V (vs. RHE) of Co-NC and Pt/C, respectively, suggests higher ORR catalytic activity. To further assess the ORR activities of the tested catalysts, we recorded the linear sweep voltammetry (LSV) polarization curves (Figure 5a). The onset potentials (E_{onset}) of Co-NOPC, Co-NC, and Pt/C were 0.95 V, 0.92 V, and 0.98 V (vs. RHE) respectively. The potential at which the reduction current sharply decreases on the LSV curves is known as E_{onset}. Experimentally, we used cross-point potential of tangent lines from the rising current and baseline current to determine the onset potential of the reaction. The half-wave potential ($E_{1/2}$) of Co-NOPC (0.86 V) is obviously improved compared to that of Co-NC (0.82 V) and even compares favorably to commercial Pt/C catalyst (0.85 V). Additionally, the Tafel slope – calculated from the LSV curves – of Co-NOPC (72 mV) is significantly lower than that of Pt/C (91 mV) confirming Co-NOPC is an efficient ORR catalyst with improved reaction kinetics compared to Pt/C (Figure 5b). The enhanced steady-state diffusion current density (j_L = 5.2 mA cm^{-2}) of Co-NOPC is comparable to that of commercial Pt/C (5.3 mA cm^{-2}). The lower overpotential and larger limit current density from Co-NOPC is attributed to its ordered hierarchical macro/meso/microporosity

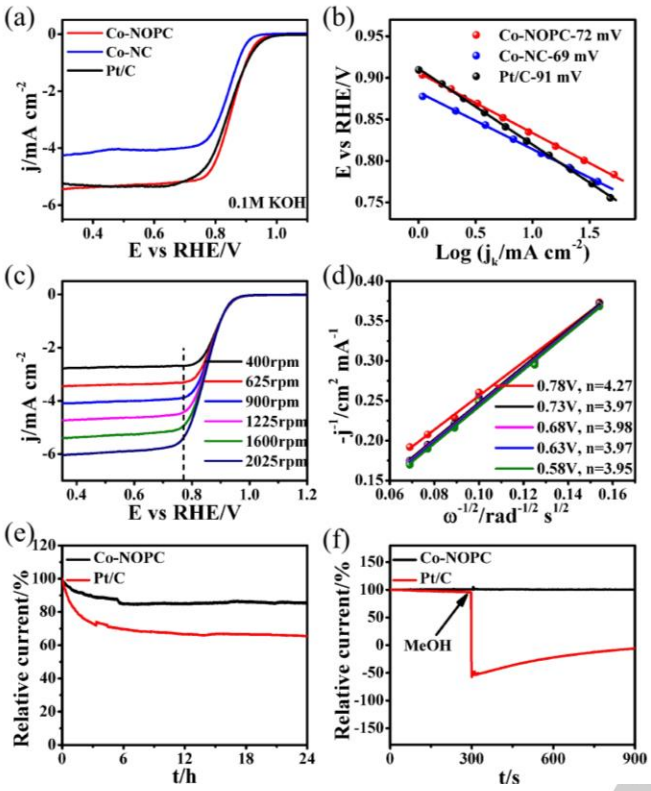

Figure 5. (a) ORR polarization curves of samples in O_2 saturated 0.1 M KOH solution with a scan rate of 10 mV s^{-1} and (b) Tafel plot of corresponding polarization curves. (c) LSV curves of Co-NOPC at different rotating speeds with a scan rate of 10 mV s^{-1} and (d) the corresponding Koutecky-Levich plots. (e) Chronoamperometric response and (f) methanol crossover tests chronoamperometric response of Co-NOPC and Pt/C at half-wave potential in 0.1 M KOH.

leading to more exposed active sites and accelerated mass transfer.[33] The influence of the hierarchical porosity is clearly noticeable when comparing the steady state current from Co-NOPC and Co-NC. On the other hand, the small Tafel slope and the positive E_{onset} may originate from the high intrinsic activity of Co-N_x (the coordinated structure of Co with the pyrrolic/pyridinic N), where N-coordinated Co sites serve as the ORR catalytic active sites.

To further improve the catalytic activity, we explored the influence of the annealing temperature and of the ratio of precursors: $Co(NO_3)_2{\cdot}6H_2O$ and 2-methylimidazole. The control of annealing temperature is indeed likely to modify the formation of active sites and carbon phase of the substrate material. Figure S11 shows that both the onset potential and the half-wave potential are reduced with increasing annealing temperature. To get additional understanding of the influence of temperature, we characterized the samples synthesized at different temperatures by XRD analysis, BET surface area determination, Raman spectroscopy, and XPS analysis. The presence of apparent Co patterns of Co-NOPC-600 and Co-NOPC-700 (Figure S4) indicates that the reduction of the Co^{2+} to Co^0, implying a significant reduction of active sites Co-N_x (Figure 4d) when the annealing temperature exceeded 600 °C, which matches well with the XPS (Figure 4) and Raman spectra observations (Figure S6), where the defect sites in the carbon phase decrease with increasing temperature.[34] In addition, the reductions of specific surface area and average pore size with enhanced temperature (Figure S5) suggest that higher temperature is responsible for the partial shrinkage of the material structural frame resulting on the reduced mass transfer. Besides the annealing temperature, the mass ratio of $Co(NO_3)_2{\cdot}6H_2O$:2-methylimidazole also influences the density of active sites because the coordination structure of ZIF-67 will translates, at the end, into tunable catalytic activity. Our analyses of the relationship between pyrrolic/pyridinic N content (Figure S9c) and the half-wave potential (Figure S12) support the fact that Co-N_x active sites play a central role in delivering high ORR catalytic performance.

Next, we investigated the reaction mechanism from Co-NOPC by determining the number of electrons involved in the reaction of oxygen. According to the Damjanovic model, a direct $4e^-$ pathway, involving reduction of O_2 to H_2O, is more efficient than a $2e^-$ pathway, in which O_2 is reduced to H_2O_2 and further to H_2O sequentially. Hence LSV curves tested at various rotating speeds were used to evaluate the ORR kinetics of Co-NOPC and Pt/C (Figure 5c). The fitted Koutecky-Levich (K-L) plots of Co-NOPC ranged from 0.78 to 0.58 V (vs. RHE) indicates that the reaction on Co-NOPC follows the desirable $4e^-$ reaction pathway and negligible formation of H_2O_2 during the ORR process (Figure 5d). The electron transfer mechanism and the formation of peroxide intermediates on Co-NOPC during ORR were also monitored by rotating ring-disk electrode (RRDE) measurements. Based on the recorded ring and disk and ring currents (Figure S13a, b), the average transferred electron number (n) was 3.93 and the yield of H_2O_2 is limited to less than 5% (Figure S13c, d), proving that the four-electron reaction pathway is proceeding under alkaline conditions.

To verify the practical applications of the catalysts, chronoamperometric measurements were used to evaluate their selectivity and long-term durability in O_2-saturated 0.1 M KOH solution at the half-wave potential of 0.86 V.[35] For long-term durability, Co-NOPC exhibits minimal loss of activity with a retention of 85% after 24 h, which is significantly larger than commercial Pt/C that exhibits an 69% retention, corresponding to 2-fold larger loss of activity (Figure 5e).[36] To assess the consequences of methanol crossover on the performance of Co-NOPC, 10 mL of methanol was instantaneously added to 100 mL of 0.1 M KOH solution to investigate methanol tolerance of catalysts during the chronoamperometric measurements (Figure 5f).[37] Upon the addition of methanol, the current of commercial Pt/C encounter a reversal from negative to positive, where the reaction on the electrode is transformed from ORR into methanol oxidation reaction (MOR). On the other hand, only a slight vibration was observed for Co-NOPC, implying its greater resistance to methanol oxidation. In conclusion, the enhanced catalytic performance from Co-NOPC towards ORR in terms of a lower overpotential, a larger diffusion controlled current density, and a reduced Tafel slope, are attributed to the large surface area exposed superior density of exposed active sites and the ordered hierarchical macro-microporous structure promoted mass transfer. On the other hand, the almost ideal four-electron transfer pathway and excellent long-term durability of Co-NOPC is due to the preference formation of Co-N_x by in-situ pyrolysis at mild temperature. Excessive annealing temperature leads to progressive inactivation of active sites, while optimized ratio of precursor is found beneficial for the formation of Co-N_x structure.

While the investigation of the ORR activity in alkaline environment allows screening the electrocatalyst candidates, proton-exchange membrane fuel cells (PEMFCs) requires the use of ORR electrocatalysts that can also efficiently operate in acid medium. This inspired us to further explore the electrocatalytic ORR performance of the Co-NOPC in acid solutions using O_2-saturated 0.5 M H_2SO_4. The CV curves of the different samples are shown in Figure S14, and the LSV polarization curves and corresponding Tafel slopes are illustrated in Figure 6a and Figure 6b. The half-wave potentials of Pt/C, Co-NOPC, and Co-NC were 0.82 V, 0.76 V, and 0.72 V, respectively. Remarkably minimal gap between the catalytic activities of Co-NOPC compared to that of commercial Pt/C was observed. We also observed a substantial improvement compared to Co-NC clearly demonstrating the Co-NOPC with controlled porosity can be an efficient catalyst for ORR operated for operating ORR in acidic conditions. Both RDE (Figure S15a, b) and RRDE (Figure 6c, d) investigations were employed to reveal the desirable 4e$^-$ reaction pathway of Co-NOPC for ORR. The number of transferred electrons and the percentage of H_2O is found to be close to 4e$^-$ and lower than 5 % respectively at low overpotential – closed to the values measured for commercial Pt/C. Finally, the long-term tolerance and anti-methanol performance of Co-NOPC reveal its potential for practical applications for ORR in acid solution (Figure S15c, d).[15]

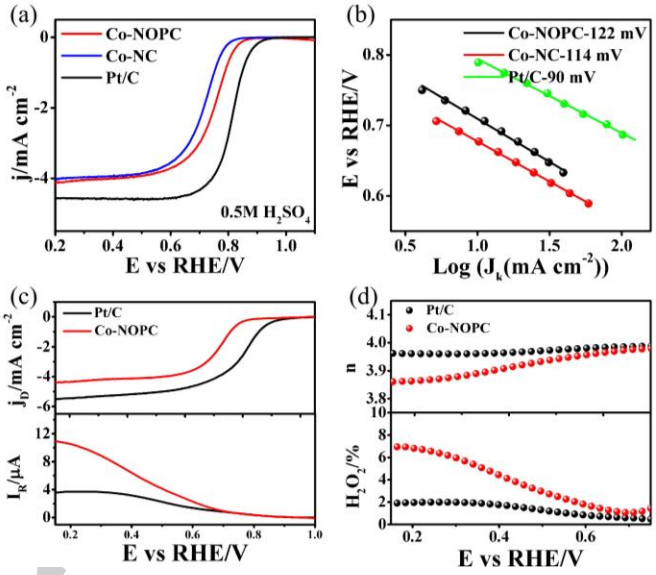

Figure 6. (a) ORR polarization curves of samples in O_2 saturated 0.5 M H_2SO_4 solution with a scan rate of 10 mV s^{-1} and (b) the Tafel plot of corresponding polarization curves. (c) The disk current and the ring current of Co-NOPC and Pt/C. (d) The electron transfer number and the hydrogen peroxide yield calculated based on the corresponding RRDE data.

Conclusions

In summary, we demonstrated the synthetic method of ordered porous ZIF-67 using hard template and ultrasonic nucleation, followed by carbonization to obtain cobalt-supported nitrogen-doped three-dimensional ordered porous carbon with controlled hierarchical porosity. Compared to Co-NC derived from the original ZIF-67, the three-dimensional ordered porous structure of Co-NOPC display ordered hierarchical macro-microporous structure with higher specific surface area to maximize the density of exposed active sites while allowing excellent mass transfer. ORR performance tests showed that

the half-wave potential of the final catalyst Co-NOPC (0.86 V) surpasses that of the state-of-the-art Pt/C catalyst (0.85 V) in alkaline solutions. Remarkably, the ORR activity in acidic have demonstrated a substantial improvement of the ORR for Co-NOPC compared to Co-NC. The superior ORR activity originates from the optimization of the density of Co-N_x active sites in the materials and the controlled hierarchical porosity of the structure that induce both improved half-wave potential and diffusion limited current density. Long-term tolerance and stability against methanol crossover in acidic and basic media make Co-NOPC an affordable alternative of Pt/C. Overall our results demonstrate a novel practical strategy for modifying MOF-derived materials for ORR. We expect such strategy can be extended to other electrocatalytic reactions for which the performances are limited by poor diffusion of the reactants to the active sites.

Experimental Section

Materials. All the chemicals used in the experiment were analytical purity and no further purification was made. 2-methylimidazole (98%), cobalt nitrate hexahydrate ($Co(NO_3)_2{\cdot}6H_2O$, 98%), potassium persulphate ($K_2S_2O_8$, 99%) and potassium hydroxide (KOH, 99.99%) were purchased from Aladdin (Shanghai, China). Nafion solution (5%), polyvinyl pyrrolidone (PVP, 30 k), sodium hydrate (NaOH, 96%) and isopropanol (99.7%) were supplied by Sigma-Aldrich (Shanghai, China). Methanol (CH_3OH, 99%), sulphuric acid (H_2SO_4, 98%), styrene (99%) and tetrahydrofuran (THF, 99%) were obtained from Sheng Jie Yi Xuan Trade Co. Ltd. (Urumchi, China). Pt/Vulcan (Pt loading 20%, Premetek, U.S.) sample labeled as Pt/C obtained from Sigma-Aldrich (Shanghai, China) was used to evaluate catalytic activity as benchmark for ORR. Deionized water (≥18.2 MΩ) was prepared using a Simplicity®UV system and used for the preparation of all aqueous solution.

Synthesis of 3D ordered PS template. The 3D ordered polystyrene sphere (PS) template with a particle diameter of 110 nm were synthesized according to the following procedure. Firstly, 50 mL of washed styrene, 400 mL of deionized water and 1.5 g of PVP were added into a 1 L flask. Then the mixture was bubbled with nitrogen for 10 min and stirred at 92 °C for 30 min. Subsequently, 50 mL of 1 wt.% $K_2S_2O_8$ was added into the flask to initiate the polymerization reaction of styrene. After keeping stirring at a rotation rate of 400 rpm for 24 h at this temperature, the mixture was cooled down and the obtained milk-like product was the monodispersed colloidal polystyrene spheres. The monodispersed polystyrene spheres were further filtered to form filter cakes. Finally, the 3D ordered PS templates were obtained after further washing with deionized water and drying at 60 °C for overnight.

Synthesis of OP-ZIF-67 and Co-NOPC. 4.5 g of $Co(NO_3)_2{\cdot}6H_2O$ and 6 g of 2-methylimidazole were added to 60 mL of methanol and fully mixed by stirring. Then, the PS template was soaked in the above solution and treated by ultrasound for 30 s to nucleate. After 24 h of static growth at room temperature, the bulk composite of ZIF-67@PS was formed after further dried at 40 °C. The obtained ZIF-67@PS was then dissolved in THF for 12 h to removed PS. After multiple centrifuging, washing and drying at 110 °C, the ordered porous ZIF-67 (OP-ZIF-67) was collected. Under nitrogen, the blue precursor was carbonized at 500 °C for 2 h to obtain cobalt-supported, nitrogen-doped 3D ordered porous carbon (Co-NOPC). For comparison, control samples, named as Co-NOPC-1:4, Co-NOPC-2:4, Co-NOPC-3:4, Co-NOPC-4:4 were prepared by adding $Co(NO_3)_2{\cdot}6H_2O$ (*n*) and 2-methylimidazole (*m*) with different mass ratios: *n:m*. Co-NOPC-500, Co-NOPC-600 and Co-NOPC-700 was synthesized with the same mass ratio at 3:4 of $Co(NO_3)_2{\cdot}6H_2O$ and 2-methylimidazole but different temperatures of 500 °C, 600 °C and 700 °C, respectively.

Synthesis of ZIF-67 and Co-NC. For comparison, conventional ZIF-67 and carbonation derivative (Co-NC) were also synthesized according to the following procedure. Firstly, 4.5 g of cobalt nitrate hexahydrate and 6 g of 2-methylimidazole were dissolved in 250 mL of methanol. After full mixing, the mixed solution was treated under ultrasonic for 20 min to nucleate and then stirred at room temperature and pressure for 12 h. Finally, ZIF-67 was obtained by several times washing with methanol, centrifugal collection and drying at 110 °C. The precursor of conventional ZIF-67 was annealed at 500 °C for 2 h with nitrogen protection to obtain Co-NC.

Structural characterization. Morphology and the microstructure of the prepared samples were characterized on a field emission scanning electron microscope (SEM; Zeiss Supra55 VP, Germany) and a high-resolution transmission electron microscope (HRTEM; Bruker Nano GmbH Berlin, Germany), which were both equipped with an energy dispersive X-ray spectroscope (EDS). Wide-angle X-ray diffraction (XRD) was performed by a Bruker D8 Advance X-ray diffractometer (Germany) with Cu Kα (λ = 0.15418 nm). Nitrogen adsorption-desorption measurements were performed on an Autosrob-1 (Quanta chrome INSTRUMENTS). The pore size distributions and specific surface areas were calculated by BJH method based on desorption branch, and the Brunauer-Emmett-Teller (BET) method, respectively. Raman spectroscopy measurements were characterized with a high-resolution laser confocal microscopy Raman spectrometer (Horiba evolution) with a 532 nm excitation laser. X-ray photoelectron spectroscopy (XPS) was recorded on a Thermo SCIENTIFIC ESCALAB 250 using 150 W Al Kα radiation.

Electrochemical characterization. All electrochemical measurements were carried on PGSTAT 302N (Metrohm Auto Lab) and a standard electrochemical cell (Pine Instrument) in an O_2 saturated electrolyte at room temperature (18- 25 °C). The counter and reference electrodes were a platinum wire and Ag/AgCl/3M KCl, respectively. RHE calibration was performed in the high purity hydrogen saturated electrolyte with a Pt foil as the working electrode and a Pt wire as the counter electrode. Cyclic voltammetry (CV) was ran at a scan rate of 1 mV s^{-1}, and the average of two potentials at which the current cross zero was taken as

thermodynamic potential for the hydrogen electrode reactions (Figure S1). The potential measured against an Ag/AgCl electrode was converted to the potential versus the reversible hydrogen electrode (RHE) according to E(RHE) = E(Ag/AgCl) + 0.976 V in 0.1 M KOH, and E(RHE) = E(Ag/AgCl) + 0.240 V in 0.5 M H_2SO_4. All data were presented without *IR* compensated.

To prepare the working electrode, 10 μL catalysts inks (6 mg mL^{-1}), prepared by dispersing 6 mg of catalysts (including Pt/C) in 1 mL of mixture solution (water: isopropanol = 1:2) with 0.1 wt% Nafion as binder, was deposited on the polished Φ5 mm glass carbon electrode (RDE, Pine Instrument). Linear sweep voltammetry (LSV) was used to characterize catalytic activity with sweep rates of 10 mV s^{-1} at a rotation rate of 1600 rpm in the O_2-saturated solution. Then the ORR polarization curves were corrected by subtracting the background current measured under N_2 atmosphere. The durability of catalysts was evaluated by performing chronoamperometric measurements at half-wave potential for 24 h. To evaluate the methanol tolerance of catalysts, 10 mL of methanol was added into 100 mL of electrolyte during the chronoamperometric measurement. For the Tafel plot, the kinetic current was calculated from the mass-transport correction of RDE by:

$$j_K^{-1} = j^{-1} - j_L^{-1}$$

Calculation of electron transferred number for ORR. The electron transfer numbers per oxygen molecule for oxygen reduction in 0.1M KOH and 0.5M H_2SO_4 are calculated by Koutechy-Levich (K-L) equation:

$$j^{-1} = j_K^{-1} + j_L^{-1} = j_K^{-1} + (B\omega^{1/2})^{-1}$$

$$B = 0.62nFC_0D^{2/3}u^{1/6}$$

$$j_K = nFkC_0$$

where j is the measured current density; j_L is the diffusion limited current; j_K is the kinetic current density; ω is the electrode rotation rate; B is the slope of the K-L plots; n represents the transferred electron number per oxygen molecules; F is the Faraday constant (F = 96485 C mol^{-1}); D is the diffusion coefficient of O_2 in 0.1 M KOH solution (D = 1.9×10^{-5} cm^2 s^{-1}); u is the kinetic viscosity of the electrolyte (u = 0.01 cm^2 s^{-1}). C_0 is the bulk concentration of O_2 (C_0 = 1.2×10^{-6} mol cm^{-3}). The total electron-transfer number (n) and hydrogen peroxide yield ($\%H_2O_2$) were determined by the RRDE approach using:

$$n = 4j_D / [j_D + (j_R / N)]$$

$$\%H_2O_2 = 100[(2j_R / N) / (j_D + (j_R / N))]$$

where j_D and j_R are the voltammetric currents at the disk and ring of electrode, respectively. N determined to be 0.37 is the RRDE collection efficiency determined.

Acknowledgements

This work was supported by the National Natural Science Foundation of China (21677171, 21978111).

Keywords: Cobalt • Electron transfer • Fuel cell • Oxygen reduction reaction • ZIF-67

[1] a) X. Wang, Z. Li, Y. Qu, T. Yuan, W. Wang, Y. Wu, Y. Li, *Chem* **2019**, *5*, 1486-1511; b) N. Shilpa, A. Nadeema, S. Kurungot, *ChemSusChem* **2019**; c) X. Huang, T. Shen, T. Zhang, H. Qiu, X. Gu, Z. Ali, Y. Hou, *Adv Energy Mater* **2019**, 1900375.
[2] Z. Zhang, J. Sun, F. Wang, L. Dai, *Angew Chem Int Ed* **2018**, *57*, 9038-9043.
[3] H. Shen, E. Gracia-Espino, J. Ma, H. Tang, X. Mamat, T. Wagberg, G. Hu, S. Guo, *Nano Energy* **2017**, *35*, 9-16.
[4] Y. Wang, W. Qiu, E. Song, F. Gu, Z. Zheng, X. Zhao, Y. Zhao, J. Liu, W. Zhang, *Natl Sci Rev* **2018**, *5*, 327-341.
[5] C. Zhu, Q. Shi, B. Z. Xu, S. Fu, G. Wan, C. Yang, S. Yao, J. Song, H. Zhou, D. Du, S. P. Beckman, D. Su, Y. Lin, *Adv Energy Mater* **2018**, *8*, 1801956.
[6] C. Spori, J. T. H. Kwan, A. Bonakdarpour, D. P. Wilkinson, P. Strasser, *Angew Chem Int Ed* **2017**, *56*, 5994-6021.
[7] J. M. : H. B. Yang, S.-F. Hung, J. Chen, H. B. Tao, X. Wang, L. Zhang, R. Chen, J. Gao,, L. D. H. M. Chen, B. Liu, *Sci Adv* **2016**, *2*, e1501122
[8] a) Z. Yang, Y. Wang, M. Zhu, Z. Li, W. Chen, W. Wei, T. Yuan, Y. Qu, Q. Xu, C. Zhao, X. Wang, P. Li, Y. Li, Y. Wu, Y. Li, *ACS Catalysis* **2019**, *9*, 2158-2163; b) C.-Y. Su, H. Cheng, W. Li, Z.-Q. Liu, N. Li, Z. Hou, F.-Q. Bai, H.-X. Zhang, T.-Y. Ma, *Adv Energy Mater* **2017**, *7*, 1602420.
[9] J. Li, M. Chen, D. A. Cullen, S. Hwang, M. Wang, B. Li, K. Liu, S. Karakalos, M. Lucero, H. Zhang, C. Lei, H. Xu, G. E. Sterbinsky, Z. Feng, D. Su, K. L. More, G. Wang, Z. Wang, G. Wu, *Nature Catalysis* **2018**, *1*, 935-945.
[10] a) P. Yin, T. Yao, Y. Wu, L. Zheng, Y. Lin, W. Liu, H. Ju, J. Zhu, X. Hong, Z. Deng, G. Zhou, S. Wei, Y. Li, *Angew Chem Int Ed* **2016**, *55*, 10800-10805; b) Z. Zhu, C. Chen, M. Cai, Y. Cai, H. Ju, S. Hu, M. Zhang, *Mater Res Bull* **2019**, *114*, 161-169.
[11] L. Shang, H. Yu, X. Huang, T. Bian, R. Shi, Y. Zhao, G. I. Waterhouse, L. Z. Wu, C. H. Tung, T. Zhang, *Adv Mater* **2016**, *28*, 1668-1674.
[12] a) J. Wang, Z. Huang, W. Liu, C. Chang, H. Tang, Z. Li, W. Chen, C. Jia, T. Yao, S. Wei, Y. Wu, Y. Li, *J Am Chem Soc* **2017**, *139*, 17281-17284; b) S. Wang, M. Qiao, Y. Wang, Q. Wang, G. Hu, X. Mamat, s. zhang, *Angew Chem Int Ed* **2019**.
[13] W.-L. Xin, K.-K. Lu, D. Shan, *Appl Surf Sci* **2019**, *481*, 313-318.
[14] L. Wang, X. Jin, J. Fu, Q. Jiang, Y. Xie, J. Huang, L. Xu, *Electroanal Chem* **2018**, *825*, 65-72.
[15] L. Lv, S. Kang, X. Li, J. Shen, S. Liu, *Nanotechnology* **2018**, *29*, 485402.
[16] J. Guo, M. Gao, J. Nie, F. Yin, G. Ma, *J Colloid Interface Sci* **2019**, *544*, 112-120.
[17] G. Piao, S. H. Yoon, D. S. Han, H. Park, *ChemSusChem* **2019**.
[18] K. Shen, L. Zhang, X. Chen, L. Liu, D. Zhang, Y. Han, J. Chen, J. Long, R. Luque, Y. Li, B. Chen, *Science* **2018**, *359*, 206-210.
[19] X. Sun, S. Sun, S. Gu, Z. Liang, J. Zhang, Y. Yang, Z. Deng, P. Wei, J. Peng, Y. Xu, C. Fang, Q. Li, J. Han, Z. Jiang, Y. Huang, *Nano Energy* **2019**, *61*, 245-250.
[20] J. Gu, C. S. Hsu, L. Bai, H. M. Chen, X. Hu, *Science* **2019**, *364*, 1091-1094.
[21] a) C. Feng, Z. Li, J. Wang, T. Yan, H. Dong, J. Feng, Q. Zhang, J. Sui, L. Yu, L. Dong, *Electroanal Chem* **2019**, *840*, 27-34; b) C. Wu, D. Xie, Y. Mei, Z. Xiu, K. M. Poduska, D. Li, B. Xu, D. Sun, *Phys Chem Chem Phys* **2019**, *21*, 17571-17577.
[22] H.-S. Park, S.-B. Han, D.-H. Kwak, J.-H. Han, K.-W. Park, *J Catal* **2019**, *370*, 130-137.
[23] a) J. Guo, S. Gadipelli, Y. Yang, Z. Li, Y. Lu, D. J. L. Brett, Z. Guo, *J Mater Chem A* **2019**, *7*, 3544-3551; b) L. Liu, Y. Zhang, X. Yu, *New J Chem* **2019**, *43*, 9666-9672; cJ. Zhou, Y. Dou, A. Zhou, R.-M. Guo, M.-J. Zhao, J.-R. Li, *Adv Energy Mater* **2017**, *7*, 1602643.
[24] a) X. Ma, X. Zhao, J. Huang, L. Sun, Q. Li, X. Yang, *ACS Appl Mater Interfaces* **2017**, *9*, 21747-21755; b) X. Lin, Y. Wang, T. Liu, H. Chen, Z. Jiang, Y. Chen, J. Liu, J. Huang, M. Liu, *ChemistrySelect* **2018**, *3*, 4831-4837; c) X. Wang, J. Zhou, H. Fu, W. Li, X. Fan, G. Xin, J. Zheng, X. Li, *J Mater Chem A* **2014**, *2*, 14064-14070.
[25] a) A. K. Díaz-Duran, F. Roncaroli, *Electrochim Acta* **2017**, *251*, 638-650; b) B. Huang, Y. Liu, X. Huang, Z. Xie, *J Mater Chem A* **2018**, *6*, 22277-22286.
[26] D. Yan, Y. Li, J. Huo, R. Chen, L. Dai, S. Wang, *Adv Mater* **2017**, *29*.
[27] M. Gao, Z. Y. Guo, X. Y. Wang, W. W. Li, *ChemSusChem* **2019**.
[28] L. Li, T. Tian, J. Jiang, L. Ai, *J Power Sources* **2015**, *294*, 103-111.
[29] I. S. Amiinu, X. Liu, Z. Pu, W. Li, Q. Li, J. Zhang, H. Tang, H. Zhang, S. Mu, *Adv Funct Mater* **2018**, *28*, 1704638.

[30] a) J. Shu, Q. Niu, N. Wang, J. Nie, G. Ma, *Appl Surf Sci* **2019**, *485*, 520-528; b) W. Xia, J. Zhu, W. Guo, L. An, D. Xia, R. Zou, *J Mater Chem A* **2014**, *2*, 11606-11613.
[31] X. Wen, L. Bai, M. Li, J. Guan, *ACS Sustain Chem Eng* **2019**, *7*, 9249-9256.
[32] a) Z. Yang, C. Zhao, Y. Qu, H. Zhou, F. Zhou, J. Wang, Y. Wu, Y. Li, *Adv Mater* **2019**, *31*, e1808043; b) B. Pattengale, S. Yang, S. Lee, J. Huang, *ACS Catalysis* **2017**, *7*, 8446-8453; c) K. Ai, Z. Li, X. Cui, *J Power Sources* **2017**, *368*, 46-56.
[33] S. Zhao, D. W. Wang, R. Amal, L. Dai, *Adv Mater* **2019**, *31*, e1801526.
[34] M. Ammar, S. Jiang, S. Ji, *J Solid State Chem* **2016**, *233*, 303-310.
[35] D.-H. Kwak, S.-B. Han, D.-H. Kim, J.-E. Won, K.-W. Park, *Appl Catal B-Environ* **2018**, *238*, 93-103.
[36] R. Li, X. Wang, Y. Dong, X. Pan, X. Liu, Z. Zhao, J. Qiu, *Carbon* **2018**, *132*, 580-588.
[37] P. Zhang, C. Chen, X. Zhang, Z. Jiang, J. Huang, J. Chen, *Electrochim Acta* **2019**, *298*, 570-579.

Entry for the Table of Contents

Layout 2:

FULL PAPER

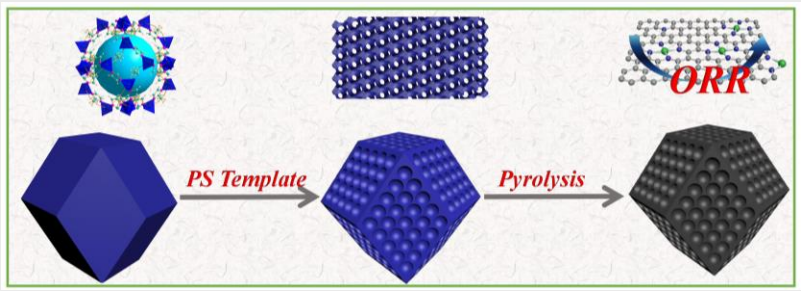

A hierarchical porous cobalt, nitrogen-doped carbon were obtained by pyrolysis of ordered porous ZIF-67, that is prepared by forced molding of a polystyrene template. The hierarchical porosity result in a significant improvement in the performance of ZIF-67 derived carbon to oxygen reduction reaction in both alkaline and acidic conditions.

Mengfei Qiao, Ying Wang, Xamxikamar Mamat, Anran Chen, Guoan Zou, Lei Li, Shusheng Zhang, Xun Hu, Damien Voiry* ,and Guangzhi Hu**

Page No. – Page No.

Rational Design of Hierarchical Porous Cobalt, Nitrogen-doped Carbon Architectures as Efficient Oxygen Reduction Reaction Electrocatalysts